

A Passive Earth-Entry Capsule for Mars Sample Return

Robert A. Mitcheltree*

NASA Langley Research Center, Hampton, Va.

Sotiris Kellas[†]

Lockheed Martin Engineering and Sciences Co., Hampton, Va.

Abstract

A combination of aerodynamic analysis and testing, aerothermodynamic analysis, structural analysis and testing, impact analysis and testing, thermal analysis, ground characterization tests, configuration packaging, and trajectory simulation are employed to determine the feasibility of an entirely passive Earth entry capsule for the Mars Sample Return mission. The design circumvents the potential failure modes of a parachute terminal descent system by replacing that system with passive energy absorbing material to cushion the Mars samples during ground impact. The suggested design utilizes a spherically blunted 45-degree half-angle cone forebody with an ablative heat shield. The primary structure is a hemispherical, composite sandwich enclosing carbon foam energy absorbing material. Though no demonstration test of the entire system is included, results of the tests and analysis presented indicate that the design is a viable option for the Mars Sample Return Mission.

Introduction

The Mars Sample Return (MSR) mission will return selected samples from Mars to Earth. The final phase of the mission requires an Earth entry, descent, and landing capsule. Since the MSR mission must be accomplished within stringent cost and mass restrictions, the Earth-entry subsystem must be both simple and low mass. In addition, the National Research Council's Task Group on Issues in Sample Return¹ determined that the potential for terrestrial contamination from Mars samples, while minute, is not zero. The sample return capsule must, therefore, assure containment of the samples. To assure containment, the capsule must either 1) include sufficient redundancy to each critical subsystem or 2) eliminate the need for that subsystem. Eliminating subsystems rather than adding redundant systems is essential for MSR because of the mass restrictions on the capsule. This paper describes the simplest and most robust option for the Mars Sample Return Earth entry capsule

The desire to obtain extraterrestrial samples for Earth-based analysis has spawned several upcoming sample return

missions with destinations other than Mars. The fourth, discovery-class mission, Stardust^{2,3} (launched Feb. 7 1999), plans to return cometary coma samples and interstellar dust in 2006. The Muses-CN mission is scheduled for a 2002 launch and will attempt to return asteroid samples in 2006. The fifth discovery class mission, Genesis, promises to collect samples of the solar wind for return in 2003. All three of these missions utilize direct entry capsules with parachute terminal descent.

Sample return missions for Mars have been studied periodically for the past 30 years⁴⁻⁶. The Earth entry phase envisioned by previous studies involved either 1) an orbit insertion at Earth with Space Shuttle or Space Station rendezvous for recovering the samples or 2) direct entry with an Apollo-style entry vehicle utilizing parachutes, air-snatch, or water recovery. The first scenario is prohibitively expensive, the second relies on fallible entry events. All of the previous studies involved entry vehicles with masses significantly larger than the current 40 kg allotment for the 2005 opportunity.

Direct entry of a passive capsule that does not include a parachute terminal descent system but relies solely on

* Aerospace Engineer, Aerothermodynamics Branch, Aerodynamics Competency, NASA Langley Research Center, Hampton Va.

[†] Aerospace Engineer V, Lockheed Martin Engineering and Sciences Co, Hampton, Va.

aerodynamics for deceleration and attitude control may represent the most robust, and least expensive entry scenario. The samples, in such a design, are packaged in hardened container(s) and surrounded by sufficient energy-absorbing material to limit dynamic loading assure during ground impact. The objective of this work is to examine one candidate Earth-entry capsule within this scenario to explore the feasibility of the approach.

The present work utilizes high-fidelity, multi-disciplinary analysis in the conceptual design phase. A combination of static and dynamic aerodynamic evaluations are supplied through new and existing wind tunnel measurements augmented by computational fluid dynamics (CFD) predictions to cover the entire entry speed range (hypersonic through subsonic). Aerothermal heating predictions, heatshield design, and thermal analysis of the entry and impact are included. Impact energy absorption is examined through crush tests and drop tests. Structural design utilizes mechanics of deformable bodies and impact tests. Ground characterization test data from the Utah Test and Targeting Range (UTTR) is included. Solid modeling is used to address packaging issues and to estimate mass properties of the vehicle. Detailed trajectory simulations and dispersion analyses are performed using the three-degree-of-freedom Program to Optimize Simulated Trajectories (POST)⁷.

After a brief description of the sample return capsule requirements, the major design drivers - as currently understood - are identified. The remainder of the paper describes analysis performed on one possible design for the capsule. The combination of these analyses point to the feasibility of this design for Mars Sample Return. This work also has direct application to future sample return missions.

System Requirements and Design Drivers

The primary requirement on the Earth-entry capsule is to assure containment of the Mars samples during the intense Earth entry, descent, and impact phase of the mission. This planetary protection concern led to the consideration of a parachute-less entry since exclusion of that descent subsystem eliminates a major vehicle failure mode and reduces mass and complexity of the vehicle. The design must also provide for easy sample recovery by providing ground recovery beacons and avoiding a water landing. Vehicle mass at launch must be less than 40 kg with a maximum dimension of 1.0 m. (Launch mass does not include the sample canisters.)

Samples of Mars rock and regolith will be hermetically sealed within two separate canisters by the 2003 and 2005 landers. These two hardened canisters, whose external surfaces will be kept uncontaminated while on Mars, will be placed in Mars orbit by the Mars Ascent Vehicle then acquired by an Orbiter for transfer into the Earth Entry capsule. (In this paper, *canister* refers to the hardened

containers of the samples, while *capsule* refers to the entire entry vehicle.) At Earth return, the capsule is spun up and released from the Orbiter for entry. After traversing hypersonic, supersonic, transonic and subsonic speed regimes the capsule will impact the ground traveling at subsonic, terminal velocity. During impact, the system must limit mechanical loads on the sample canisters below predetermined limits. In addition, the temperatures of the samples must be maintained below 325 K. Shape, size, mass, and mechanical strength of the sample canister are major drivers in the design of the Earth-entry system. For this study, the canisters are assumed to be spherical with diameter of 0.14 m and mass of 3.6 kg. These enclosures are capable of handling mechanical loads of 400 g's without degrading the science quality of the samples and 2000 g's without risk of rupture.

The capsule's relative entry velocity at 125 km altitude is between 11 and 12 km/s, depending on the Earth return trajectory. This high-energy entry drives the design to a blunt aeroshell with an ablating heat shield to protect the vehicle from the intense heating environment expected in the first 60 seconds of the entry. Aerodynamic decelerations between 40 and 80 Earth g's occur during this portion of the entry. After 100 seconds, the capsule has decelerated to around Mach 1.0 and descended to 30-35 km altitude. For the remaining 400 seconds of the entry the capsule descends at subsonic speeds. Blunt aeroshell shapes which can survive the intense heating of the hypersonic heat-pulse, often suffer aerodynamic stability problems in the transonic and subsonic regimes. The conflicting requirements of minimizing heating while maximizing subsonic aerodynamic stability is a major design trade in selecting the aeroshell shape.

Surface winds are also a major design driver. The capsule must be designed to accommodate 13 m/s sustained surface winds at impact. Winds increase the impact velocity vector and can result in off-axis impact angles.

Suggested Design

Figure 1 presents a schematic of a design based on a 1.0 m diameter, blunted, 45-degree half-angle cone forebody. The sample canisters are packaged within energy absorbing material. The primary structure is a stiff, hemispherical, composite-sandwich shell. The heatshield is 0.05 m thick PICA-15.

Canister transfer access, attachment hard points, vents, and electrical connections are "hidden" in the lower heating region of the afterbody. The canisters are positioned side by side such that a large range of primary impact angles can be handled as well as the lower energy impacts resulting from bounces. It is beyond the scope of this paper to discuss all of the trades that were examined in evolving this design. The remainder of the paper examines each element of this design to illustrate its feasibility.

Energy Absorbing Material

At impact, a complex interaction of events occurs whose sum is the removal of the kinetic energy at impact. Energy is absorbed by the ground, by the heatshield, by deformation and failure of the capsule structures, and by crush of the energy absorbing material. The goal of the design is to limit mechanical loads on the sample canister at impact. This section focuses on selection and testing of the energy absorbing material to meet that goal.

The samples, and the means which they are supported within the canister, dictate the maximum allowable deceleration load which is currently assumed 400 g's. The most efficient deceleration profile for the canister during ground impact is one which is constant at, or just below, that maximum limit. This constant deceleration represents an ideal crush response.

There are two possibilities for crush energy management in the design of the capsule to achieve an ideal crush response. In the first, the outer surface of the aeroshell (heatshield, structure, and energy absorbing material) crushes inward towards the canister. This scenario places no particular requirements on the capsule structure or the shape of the canister. Obtaining an ideal crush response, however, requires precise knowledge of the ground's impact characteristics, the structure's strength during failure, and requires a tailored strength gradient be built into the energy absorbing material. The second possibility is to design the capsule with a relatively rigid outer shell structure such that, at impact, the shell deformation is limited. The canister decelerates as it travels into the energy-absorbing material. This second approach has the disadvantages that 1) the canister shape becomes important with preference towards a spherical shape (to present a constant projected area to the energy absorbing material despite attitude at impact), and 2) the structural mass is increased. Obtaining an ideal crush response with this approach, however, is simplified. In addition, the stiff structure can be used to support attachments to the cruise stage. The second approach - a stiff outer-structure approach - is taken.

For a given impact load limit, the crush stress of the energy absorbing material depends on the projected area and mass of the canister while the required stroke depends on the velocity at impact. For example, if each sample canister is a 0.14 m diameter sphere of mass 3.6 kg, the desired crushing strength of the material is 133 psi to limit accelerations to 400 g's.

In addition to a tailorable compressive strength, the material selected for energy absorption must be a good thermal insulator and maintain its strength at elevated temperatures. It must be nearly isotropic, and be able to survive the launch environment loads. It must be thermally stable, and must be either open cell for venting in vacuum or, if closed cell, must

possess sufficient strength to avoid cell rupture in vacuum. Finally, its crush strength must be strain-rate insensitive over a large range to achieve an ideal crush response.

Honeycombs of paper, metal, polymer, and fiber reinforced plastics were considered as well as rigid, and semi-rigid foams of carbon, metal, ceramic, and plastic. The honeycombs are highly anisotropic and poor thermal insulators. Plastic foams have a small operating temperature range, and ceramics are generally heavy.

Reticulated vitreous carbon foam is an open cell material with exceptional chemical inertness, high temperature strength, and low thermal conductivity. The material has the additional benefit that its brittle failure mode is very localized and predictable. Over 200 static tests and 100 dynamic tests were performed on carbon foam samples from three manufacturers⁸. Some representative results are included here to 1) illustrate its suitability as an energy absorber, and 2) estimate the density of the material required for this application.

Carbon foam is currently manufactured at different densities and compressive strengths. Static and dynamic crush response of one form of the material is shown in Fig. 2. The static tests reveal a nearly constant strength for over 90 percent strain. (Crush stroke was limited in the dynamic tests by the available kinetic energy at impact.) To illustrate that the material strength can be "tailored" to a desired value, a planar structure was created by removing hexagonal cores from 2.5 cm thick slab of the material. The slabs were then stacked with a 0.002 m carbon foam sheet between layers to create a honeycomb-like solid whose density was 16 kg/m³. The resulting static strength of a typical sample was measured to be between 10 and 15 psi. These values are much less than the values required for the present application but this "machined" approach to tailoring the strength illustrates the extremes to which the material can be tailored.

Figure 2 reveals the compressive strength of carbon foam appears to be rate sensitive. A factor of 2.7 increase in compressive strength was measured when the crush rate was increased from 0.0004 m/s to 1.6 m/s. (Impact speeds are expected to approach 40 m/s.) Dynamic tests in vacuum revealed that the apparent rate sensitivity is not a viscous effect. The increase in strength is the interaction between the smooth indenter and the rough foam surface⁸. If a suitable coating is deposited on the foam surface which causes more of the foam to become engaged during contact, an increase in static strength, comparable to that observed in the dynamic tests, is realized. This surface coating effect is presented in Fig. 3.

Acoustic vibration tests at 140 db (0-500 HZ) for 1.5 min revealed the material can survive severe acoustic launch loads.

Increasing the carbon foam temperature from 300 K to 425 K and 525 K reveals only 20 and 28.6 percent reductions in strength respectively. (The temperature of the foam at impact should be around 300 K with a thin layer near the stagnation point approaching 400 K.)

By combining the information from all of the tests performed, an estimate of the relationship between density and strength for the material can be produced. It appears that 1) carbon foam is a suitable candidate for the energy absorbing material, 2) its strength can be tailored to desired values, and 3) an energy absorber whose strength is "tailored" to 133 psi would have density below 60 kg/m^3 and provide 90 percent usable stroke.

Ground Characterization Tests

Selecting a crush-energy-management approach based on a rigid outer shell structure removed the influence of the ground's impact characteristics on the design of the energy absorbing material. The need to understand the ground, however, remains necessary to determine the loads to design the structure.

The location for the impact is not determined. One possibility is the dry lake bed at UTTR. Dynamic impact tests were performed at UTTR using a 0.514 m diameter hemispherical penetrometer. The penetrometer contained a 500-g range, 3-axis accelerometer and was dropped from heights up to 40 m. Accelerometer data was acquired at a rate of 3200 samples per second. Table 1 presents a summary of the impact tests performed.

Diam, m	Mass, kg	V, m/s	Acc, g's
0.514	11.02	18.42	400
0.514	18.53	18.68	290
0.514	11.02	16.41	330
0.210	2.98	18.70	360
0.514	18.90	21.92	320
0.514	18.90	21.92	375
0.514	18.90	26.23	500
0.514	18.90	26.23	515
0.514	18.90	16.59	208
0.514	18.90	16.59	222

Table 1. UTTR Ground Impact Tests and Results.

In Table 1, *Acc* is the maximum acceleration recorded during the impact. Figure 4 presents four acceleration profiles from the tests. Meyer's⁹ theory provides a simplified description of plastic impacts in which the ground is assumed to exert a constant pressure on the impactor. This theory predicts maximum acceleration varies linearly with $V\sqrt{D/M}$ when penetrations are small relative to the diameter, *D*, of the penetrometer. The data in Table 1 does not match this theory. Figure 5 reveals that the maximum accelerations vary like the

hydrodynamic parameter V^2D^2/M . Meyer's theory was modified by replacing the constant ground pressure with an expression for the pressure that is quadratic in velocity. The associated constants were adjusted to match the measured data shown in Figs. 4 and 5. This theory is then used to predict the expected acceleration of a 39 m/s impact of a 0.425 m radius, 42.9 kg, rigid shell with the UTTR surface. The prediction is presented in Fig. 6. The maximum acceleration 980 g's occurs at 0.056 m penetration. The total penetration is predicted to be 0.14 m.

Structural Design

The design in Fig. 1 contains one critical structural element: the primary impact structure. The requirement for a stiff structure whose deformation is limited during impact from a large range of possible attitudes, led to the decision to utilize a near-hemispherical structure of composite sandwich construction with integral frame stiffeners. The ground characterization tests at UTTR discussed above reveal that this structure must be sufficiently strong to limit deformations during a dynamic 980 g impact. The structure will receive some cushioning from heatshield deformation and foundation support from the energy absorbing material. To estimate the heatshield contribution, crush tests were performed on samples of PICA-15 as shown in Fig. 7.

The primary spherical structure shown in Fig. 1 is a composite sandwich structure. It is required to maintain its shape during the 3 ms of loading. Its 0.001 m (outer) and 0.0015 m (inner) face sheets are 2-D triaxial braid textile (or unidirectional material arranged in a quasi-isotropic manner) of intermediate modulus graphite fiber in a polyimide-class resin. The core is 0.0175 m of 80 kg/m^3 structural foam. The 6 internal I-beam frames are made from high strength unidirectional carbon fibers in a polyimide resin. The total mass of the structure is 4.71 kg.

Dynamic finite element analysis provides the best available analytic tool for characterizing this structure's reaction to these loads but requires detailed information on the mechanical properties and failure modes of each of the elements. To populate this set of empirical constants, a series of dynamic tests were performed on 0.3 m diameter graphite-epoxy hemispherical shells and sandwich structures. Figure 8 compares the crush response of 0.001 m graphite-epoxy shells under static and dynamic tests. The complete design of the structure using dynamic finite element analysis was incomplete at the time of writing of this paper. A simpler method to illustrate the adequacy of this structure for the purposes of this feasibility study involves static strength of material analysis.

From the UTTR ground characterization tests, the estimate of the acceleration profile of the capsule is shown in Fig. 6. By assuming the entire 42.9 kg (entry mass) of the capsule must be decelerated according to this profile, the maximum

expected load on the structure and heatshield combination is 412 kN. In addition, the degree of ground penetration and heatshield deformation at the time of that loading results in the force being exerted over a spherical section with projected diameter of 0.45 m. The average external pressure is 2279 kN/m² (330 psi). However, the energy absorbing material supports this structure so that it must support a pressure differential of only 197 psi.

The bending and membrane stresses as well as deformations of a spherical sandwich structure under this loading can be computed using the methods in Roark¹⁰. The sandwich shell provides enough strength in bending to support 546 kN before failure. The frames add an additional 115 kN capability for a combined safety factor in bending of 2.5. The frames increase the shear strength of the structure such that the combined structure has a safety factor of 5 in shear. These large safety factors are necessary since the rate of loading is sufficiently high that quasi-steady analysis is not accurate.

The secondary structure (which supports the heatshield beyond the primary structure) represents a less challenging structural design. The requirement on this structure is that its deformations under aerodynamic deceleration loads are limited to values that will not risk fracture of the heatshield. This "wing" structure need not survive the ground impact. Ideally, at impact it would shear off decreasing the mass that the primary structure must decelerate. It is also available to provide energy absorption in the event of large off-axis impact attitudes. The design is a variation on a sandwich structure with the outer face sheet of 0.8 mm graphite polyimide just behind the heatshield. The void between this face sheet and the spherical structure is filled with structural foam of density 40 kg/m³ or less. A prediction of the forebody pressure distribution at the maximum pressure point in the trajectory is shown in Fig. 9. s is the distance along the surface from the geometric stagnation point. (This CFD prediction is discussed in the *Aerothermodynamics* section.) The compressive loads on this portion of the structure are around 3 psi.

Aerodynamics

Aerodynamic drag and stability of the design in Fig. 1 are required in hypersonic, supersonic, transonic, and subsonic flight regimes. The selection of the 45 degree half-angle cone aeroshell was the result of a trade among hypersonic drag (heating), subsonic drag (impact velocity) and subsonic stability (available crush stroke).

Figure 10 presents an approximation of the drag coefficient across the Mach range for the 45-degree half-angle shape. The hypersonic value, 1.07, was computed at Mach 31.8 and 21.5 using the Langley Aerothermodynamic Upwind Relaxation Algorithm (LAURA)¹¹. (These solutions are described in the *Aerothermodynamics* section.) The subsonic

value, 0.65, comes from tests conducted in the Langley 20-foot Vertical Spin Tunnel¹². The supersonic and transonic values are from Brooks¹³ and Nichols¹⁴ wind tunnel data on a similar geometry. For the purposes of this feasibility study, the important values are the hypersonic value, which affects the heat pulse, and the subsonic value that determines the impact velocity.

Aerodynamic stability is a function of aeroshell shape and mass properties. A solid model of the design shown in Fig. 1 predicts the c.g. to be 0.266 m back from the nose. The spin-axis inertia is 3.33 kg-m². The pitch and yaw inertia are 2.03 and 2.13 kg-m² respectively. Aerodynamic stability is comprised of a static and dynamic component. For static stability, the slope of the moment curve at this c.g. location, $C_{m,\alpha}$ must be negative at the trim angle of attack (0° for this design). Figure 11 presents the variation in this parameter with Mach number. Static stability is highest in the hypersonic region (large negative $C_{m,\alpha}$). Static stability decreases near Mach 3 as the sonic line jumps from the nose to the shoulder of the vehicle. In addition to the decrease in static stability indicated by $C_{m,\alpha}$, dynamic stability decreases at lower speeds and can become unstable in the transonic and subsonic flight regimes. If a vehicle is stable in the low subsonic speed regime, it will typically be stable at higher speeds. To examine the dynamic stability of blunt aeroshells considered for this design, a set of six mass-scaled spin-tunnel models were tested¹². Figure 12 presents one attitude time history for a model geometrically similar to that shown in Fig. 1. The figure captures a test period immediately following a 35-degree intentional perturbation on the model and reveals the oscillations are decaying. The model is stable and the oscillations diminish to a limit cycle amplitude of less than 10 degrees. Moving the model's c.g. location further from its nose results in increased limit cycle amplitude and decreased amplitude of survivable perturbations.

Entry Trajectory and Landing Footprint

The geometry of the Earth approach trajectory is uncertain at this time. For this study, the exoatmospheric trajectory is assumed to have a V_∞ of 2.96 km/s, declination of -48.3 degrees, and right ascension of 284.9 degrees. This approach geometry results a retrograde atmospheric entry with a relative velocity of 11.77 km/s at 125 km altitude.

Figure 13 presents the velocity and altitude time history associated with entry of the 42.9 kg capsule in Fig. 1 for an inertial flight path angle of -11.8 degrees. This entry angle was selected as the result of a trade between heatshield mass and maximum surface pressure. The maximum acceleration of 57.3 g's occurs at an altitude of 49.8 km, 38 seconds after the 125 km altitude atmospheric interface. Peak heating occurs at 32 seconds and 58.95 km altitude. After 86 seconds, the capsule has decelerated to Mach 1 and descended to 32.7 km altitude. The capsule attains terminal velocity shortly

thereafter and impacts the ground (altitude = 1.3 km) at $t = 438$ seconds at a flight path of -90 degrees (vertical) while traveling 39 m/s.

An estimate of the landing footprint is produced by varying mass, flight path angle, atmospheric properties and aerodynamic drag. The mass was varied plus or minus 1.25 kg ($3\text{-}\sigma$) around a nominal 42.9 kg value. Flight path angle was varied plus or minus 0.07 degrees which corresponds to the uncertainty associated with releasing the capsule 18 hrs prior to atmospheric interface. The Global Reference Atmospheric Model - 1995 (GRAM-95) was used to obtain variations in density, pressure, and winds. Aerodynamic drag was varied plus or minus 5 percent in the hypersonic and subsonic regimes and 10 percent in the supersonic and transonic regimes. The resulting footprint for a 2500 case Monte-Carlo simulation overlaid on latitude and longitude of a UTTR landing site is shown in Fig. 14. The $3\text{-}\sigma$ landing ellipse is 40 km down range by 20 km cross range. If the capsule is separated from the Orbiter 42 hrs prior to atmospheric interface, larger uncertainties in the flight path angle result in an increase the downrange component to 70 km.

Aerothermodynamics, Heatshield, and Thermal Analysis

An estimate of the stagnation-point, non-ablating heating associated with the entry trajectory is shown in Fig. 15 (entry mass is 42.9 kg). The convective heating estimate comes from Chapman's equation and the radiative heating comes from the method of Tauber and Sutton¹⁵. The CFD predictions for convective heating are discussed below. Peak heating is predicted to be 747 W/cm² by the engineering approximations of which 616 W/cm² is convective. The stagnation point heat load is 10540 J/cm² from convective plus 860 J/cm² radiative for a total of 11400 J/cm².

The maximum heating point ($t=32$ s) and the maximum deceleration point ($t = 38$ s) in the heat pulse were computed using the LAURA CFD code¹³. An 11 species, thermochemical nonequilibrium gas-kinetic model with fully catalytic, radiative equilibrium wall boundary condition was used. The axisymmetric computational grid has 40 points along the body and 64 points normal to the surface with the first grid cell having a cell Reynolds number of 2. The non-ablating stagnation point heating predicted at the maximum heating and pressure points in the trajectory are shown as the circle symbols in Fig. 15, and the prediction for the entire forebody (assumed laminar) is shown in Fig. 16. The CFD prediction is 5 percent higher than the engineering estimate at peak heating and 0.6 percent higher at maximum pressure.

The flight Reynolds numbers based on diameter for these two cases are 223,100 and 435,700. (The peak Reynolds number during the heat pulse is 561,500 at a point where the heating

has dropped to 11 percent of its peak value.) One indicator of the potential for transition to turbulence is the momentum thickness Reynolds number, Re_{θ} . Figure 17 presents values for the momentum thickness Reynolds number extracted from the two CFD solutions. A criteria for transition commonly used is 250. The figure indicates the Reynolds number effects may induce transition on the conical flank late in the heat pulse. Surface roughness and ablation out-gassing can also produce transition. A CFD solution using the Baldwin-Lomax turbulence model was generated at the maximum pressure location in the trajectory. The transition location was specified as the juncture between the spherical nose and conical frustum location ($s = 0.3$ m). That solution predicted convective heating on the flank of the body (which typically is a factor of 2.2 lower than the stagnation point value) to increase by a factor of 3.8 which results in flank heating 70 percent higher than the stagnation point value. If transition does not occur until peak heating, the integrated heat load to the flank of the vehicle and the required heatshield thickness is still less than the stagnation point. The question of transition must be examined closer. For the purposes of this study, a constant heatshield thickness sized for the laminar stagnation point heating environment is used over the entire forebody.

Phenolic Impregnated Carbon Ablator (PICA-15) is chosen as the candidate heatshield material. It is a lightweight ablator with density of 227 kg/m³. To determine the required thickness, the estimate for total heating in Fig. 15 is increased by 20 percent (peak becomes 896 W/cm² and heat load becomes 13681 J/cm²). The thickness required is also a function of maximum allowable temperature in the underlying structure. Polycyanate structures have specified 520 K as the maximum allowable temperature. The graphite polyimide structure has multiple use temperature limits of 540 K and single use limit up to 643 K. Figure 18 presents the relationship between heatshield thickness and maximum bond line temperature predicted by the FIAT¹⁶ material response code for this heat pulse. To limit bond line temperatures behind the heatshield to 520 K, the required heatshield thickness for these conditions is 0.0366 m. To limit bond line temperatures to 640 K requires only 0.0243 m of heatshield. The design in Fig. 1 provides 0.05 m of PICA 15 so includes not only the 14-20 percent margin on heating but 37 to 100 percent on thickness. This large margin will decrease if entry velocity increases.

The afterbody thermal protection system has not been examined in detail. The maximum heating on the afterbody is typically less than 5 percent of the forebody (results in an estimate of peak at 35 W/cm² and heat load of 680 J/cm²). Large margins (factor of 3) are typically placed on afterbody heating predictions. A material such as SLA-561V (density 264 kg/m³) as used on the afterbody of the Stardust Sample Return Capsule² may be an appropriate material. For mass purposes, 0.011 m of SLA561V covers the entire afterbody in the design shown in Fig. 1. This thickness is greater than that

used on the Stardust afterbody that was designed for twice the heatload. The afterbody also contains penetrations for the attachment hard points, the electrical connection, vents, and the lid. The environment at each of these penetrations will be less severe than those expected on similar penetrations on the Stardust afterbody. Seals and vents designed for that mission should be adequate here.

The temperature of the sample must not exceed 370 K. A pre-impact thermal analysis was performed assuming the PICA-15 heatshield was 0.0366 *m*. thick and the capsule was at 300 K prior to entry. The predicted temperature distribution at $t = 438$ s (impact) is shown in Fig. 19. The thermal energy is just beginning to migrate into the energy absorbing material. At impact, however, the canisters crush into the heated material. A simple energy balance, which assumes the 3.6 *kg* canisters are solid aluminum and that all of the thermal energy within 1 diameter of the canister ends up in the canister, predicts the temperature rise in the canister to be 39⁰ K. If the analysis is repeated to include all thermal energy within two diameters, the temperature rise is 94⁰ K. This conservative energy balance approach did not include thermal losses to the air or the ground. During ground characterization tests, the ground temperature was measured to be 288 K.

Mission Scenario and Impact Performance

From launch through separation at Earth return, the capsule is attached to the MSR Orbiter via three attachment hard points on the afterbody of the primary spherical structure. The samples are contained in a hermetically sealed, biologically clean, canister that is transferred into the capsule on Mars orbit. This transfer and placement of the afterbody lid is accomplished via Orbiter mechanisms.

Upon Earth arrival the capsule is spun up to 2 rpm and positioned such that after separation (18-42 hrs prior to entry) the capsule enters at an inertial flight path angle of -11.8 degrees. Prior to separation, the ground recovery beacons are activated. (Each of the 2 beacons is assumed to be 0.3 *kg* which includes the 0.05 *kg* batteries necessary to supply each transmitter with 0.5 *W* of power for 24 hours.) The Orbiter performs a deflection maneuver after separation. The attachment hard point locations act as vents during entry.

Ground impact (altitude 1295 m) occurs 438 seconds after, and 490 km downrange of, atmospheric interface. The impact velocity for zero surface winds is 39 m/s. If the impacted ground is the ground examined at UTTR, the deceleration loads on the heatshield and structure will exceed 400 *g*'s within the first 0.5 millisecond causing the canisters to begin crushing into the energy absorbing material. Ten milliseconds later the entire capsule will have decelerated to the same ground-relative velocity as the canisters and their crushing into the energy absorbing material will halt having used 0.06-0.09 *m* of the available 0.16 m of stroke. The entire

capsule will come to rest 5 to 10 milliseconds later having penetrated to a depth of 0.14 *m*.

If surface winds are a sustained 13 *m/s*, the resultant velocity is 41 *m/s* and an angle of incidence of 18 *deg* will occur. In this orientation, the available stroke is 0.136 m of which 0.081-0.122 m is required.

Mass Summary

A breakdown of the mass of each element of the design is provided in Table 2. A 25 percent mass margin has been added in addition to the safety margins discussed in the previous sections.

Element	Mass, kg
Heat shield	11.19
Aftbody TPS	1.96
Primary Structure	4.71
Secondary Structures	2.96
Canisters(2)	7.20
Receptacles	1.36
Energy Absorbing Mat.	2.52
Beacons(2)	0.60
Mechanisms	1.90
Sensors and cables	0.20
Miscellaneous	1.14
Launch Total	28.53
Entry Total	35.73
Launch Total (+ 25%)	35.66
Entry Total (+25%)	42.86

Table 2. Mass of each element of the suggested design in Fig. 1.

Conclusion

A combination of analysis and testing was performed to determine the feasibility of an entirely passive Earth entry capsule for the Mars Sample Return mission. The design circumvents the potential failure modes of a parachute terminal descent system by replacing that system with passive energy absorbing material to cushion the Mars samples during ground impact. The suggested design utilizes a 1.0 m diameter spherically-blunted 45-degree half-angle forebody with a low-density, ablative heatshield. The primary structure is a frame-stiffened composite sandwich enclosing carbon foam energy absorbing material. Results of the testing and analysis presented indicate that the design with a launch mass of 35.7 kg is a robust option for the Mars Sample Return Mission.

Acknowledgments

Thanks are extended to Mark Adler of the Jet Propulsion Laboratory for supporting this work. Dr. Y. K. Chen of NASA ARC provided the heatshield sizing and pre-impact thermal analysis. Mr. David Mitcheltree and Capt. James Theiss assisted in the UTTR ground characterization tests. Nelson Seabolt constructed much of the impact test hardware including the ground penetrometers. Matt Hendrickson performed the solid modeling of the design. Mike Fremaux conducted the vertical spin tunnel tests. Ed Fasanella assisted in the structural design. Prasun Desai performed the landing footprint analysis.

References

¹Hermann, R. J., and Lineberger, W. C., "Mars Sample Return: Issues and Recommendations," Task Group on Issues in Sample Return, Space Studies Board, National Research Council, ISBN 0-309-057337, National Academy of Sciences, 1997.

²Atkins, K. L., Brownlee, D. E., Duxbury, T., Yen, C., and Tsou, P., "STARDUST: Discovery's Interstellar Dust and Cometary Sample Return Mission," Proceedings from the 1997 IEEE Aerospace Conference, Feb., 1997.

³Mitcheltree, R. A., Wilmoth, R. G., Cheatwood, F. M., Brauckmann, G.J., and Greene, F. A., "Aerodynamics of Stardust Sample Return Capsule," AIAA 97-2304, June, 1997.

⁴Williams, S. D., "A Preliminary TPS Design for MRSR - Aerobraking at Mars and at Earth," AIAA 90-0052, Jan., 1990.

⁵Meyerson, R. E., and Cerimele, C. J., "Aeroassist Vehicle Requirements for a Mars Rover/Sample Return Mission," AIAA Paper 88-0303, Jan., 1988.

⁶Gamble, J. D., "JSC Pre-Phase-A Study Mars Rover Sample Return Mission Aerocapture, Entry, and Landing Element," JSC-23230, May, 1989.

⁷Brauer, G. L., Cornick, D. E., and Stevenson, R., "Capabilities and Applications of the Program to Optimize Simulated Trajectories (POST)," NASA CR-2770, Feb. 1977.

⁸Kellas, S., "Experimental Characterization of Carbon Foam for Crash Energy Management," National Technical Specialist's Meeting on Rotocraft Crashworthiness, American Helicopter Society, Phoenix, Arizona, Sept 14-16, 1998,

⁹Goldsmith, W., *Impact*, Edwin Arnold Ltd., London, 1960.

¹⁰Roark, R. J., Young W. C., *Roark's Formulas for Stress and Strain*, 6th Edition, McGraw Hill Publishers, 1989.

¹¹Cheatwood, F. M., Gnoffo, P. A., "User's Manual for the Langley Aerothermodynamic Upwind Relaxation Algorithm (LAURA)," NASA TM-4674, Apr., 1996.

¹²Mitcheltree, R. A., Fremaux, C. M., "Subsonic static and Dynamic Aerodynamics of Blunt Entry Vehicles," AIAA Paper 99-1020, Jan. 1999.

¹³Books, J. D., "Some Anomalies Observed in Wind Tunnel Tests of a Blunt Body at Transonic and Supersonic Speeds," NASA TN D-8237, June, 1976.

¹⁴Nichols, J.O., and Nierengarten, E. A., "Aerodynamics Characteristics of Blunted Bodies," JPL TR 32-677, 1964.

¹⁵Tauber, M. E., and Sutton, K., "Stagnation Point Radiative Heating Relations for Earth and Mars," *Journal of Spacecraft and Rockets*, Vol 28., No. 1, Jan.-Feb., 1991, pp. 40-42.

¹⁶Chen, Y. K., and Milos, F. S., "Fully Implicit Ablation and Thermal Analysis Program (FIAT)," Presented at the Fourth International Conference on Composites and Engineering, Kona, HI, July, 1997.

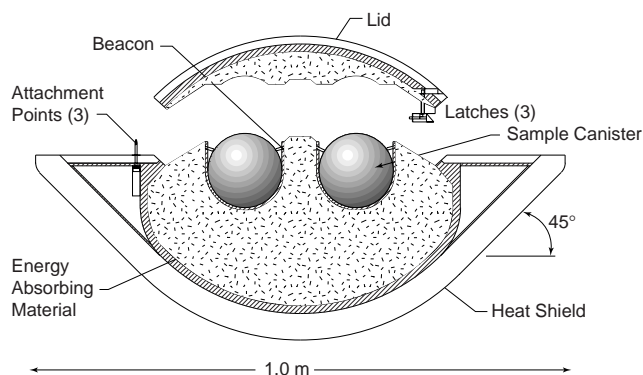


Fig 1. Schematic of entirely passive design

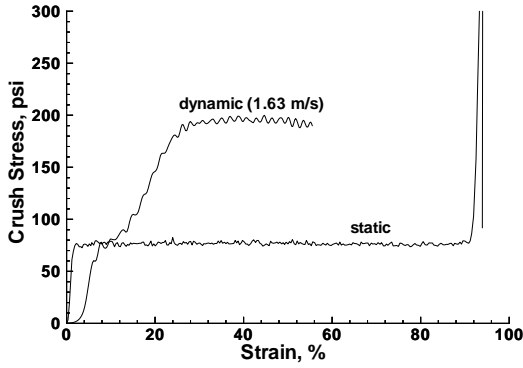


Fig. 2 Static and dynamic crushing strength of 60 kg/m³ carbon foam

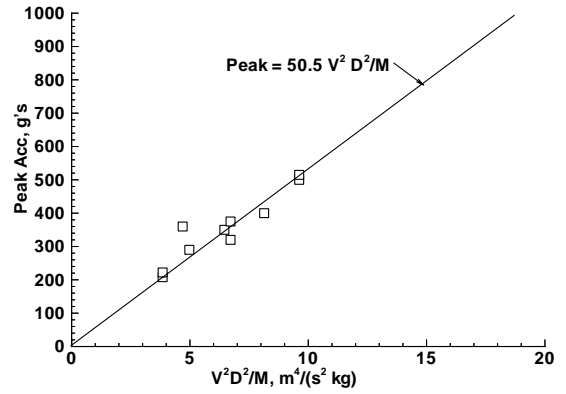


Fig 5 Variation in maximum acceleration from UTTR impact tests

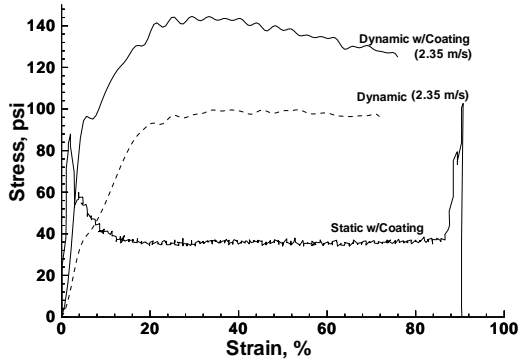


Fig. 3 Effect of surface coating on static and dynamic crushing strength of 51 kg/m³ carbon foam

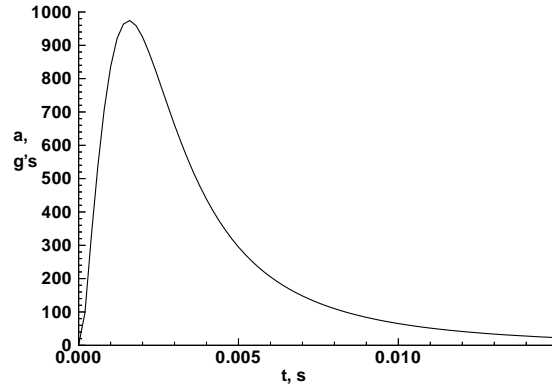


Fig. 6 Modified Meyer's law prediction of 39 m/s impact of 0.425 m radius, 43.9 kg, rigid shell with UTTR surface

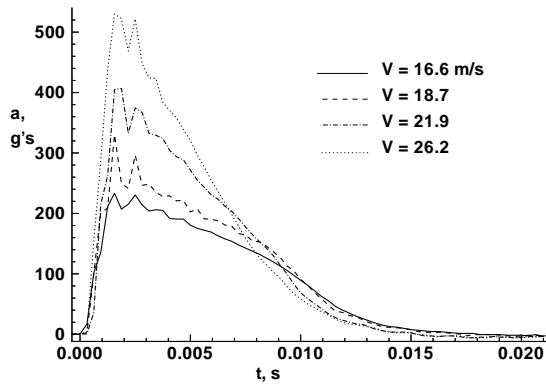


Fig. 4 Acceleration waveforms of 0.5 m, 18.5 kg penetrator impacts on UTTR surface

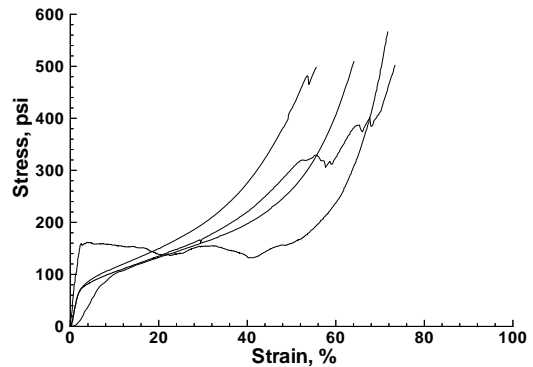


Fig. 7 Static Crush strengths of four samples of PICA-15 taken from arc-jet tested coupon.

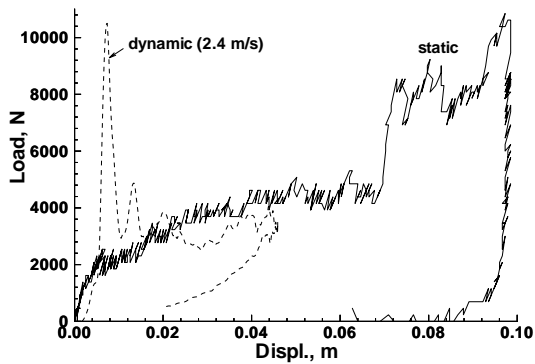


Fig. 8 Static and Dynamic crush of 0.001 m thick, 0.3 m Diameter, graphite-epoxy shells.

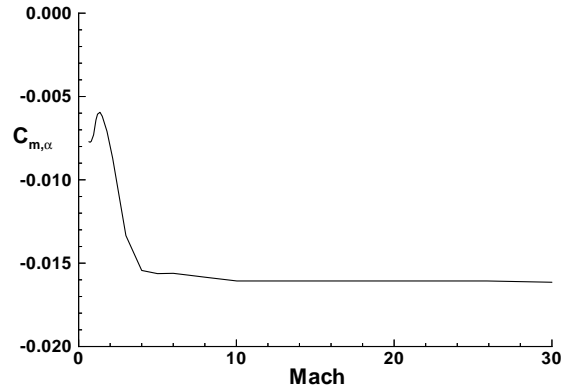


Fig 11 Moment coefficient slope variation with Mach number for 45-degree half-angle design

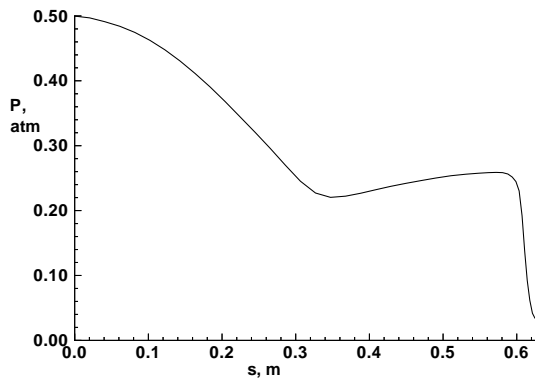


Fig. 9 Maximum forebody pressure distribution at Mach 23 for 45 degree half-angle cone design

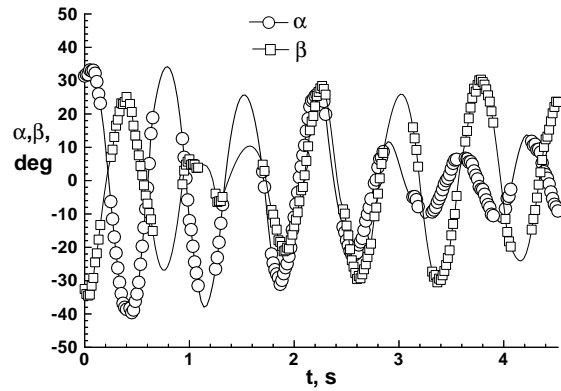


Fig. 12 Decay of large perturbation on 0.356 scale model of 45-degree half-angle design in 20-Foot Vertical Spin Tunnel

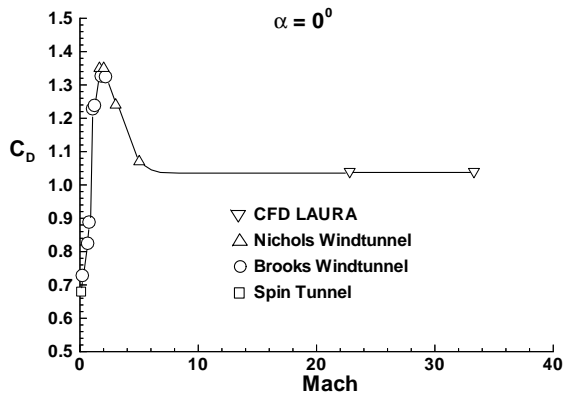


Fig. 10 Drag coefficient variation with Mach number for 45-degree half-angle design.

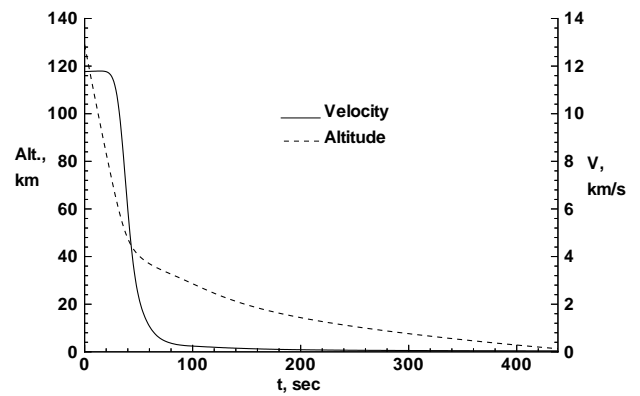


Fig. 13 Entry trajectory speed and altitude for -11.8 degree entry angle

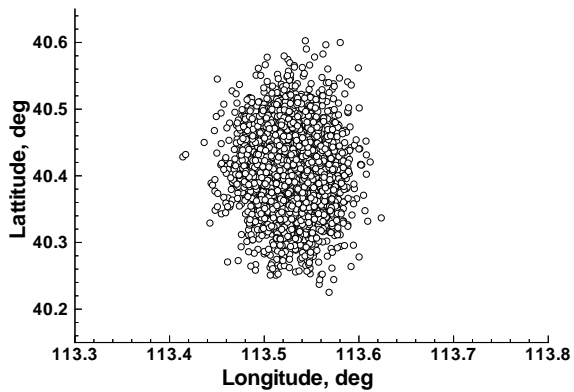


Fig. 14 Landing footprint from dispersion on entry angle, entry mass, atmosphere, and drag

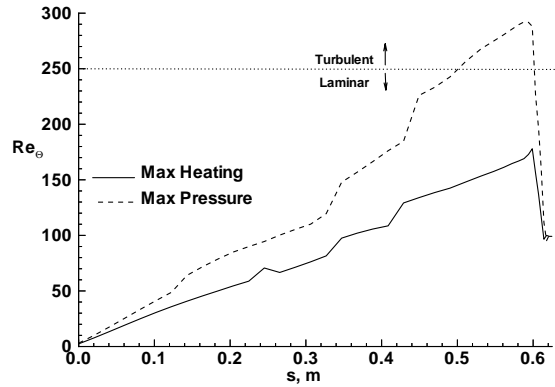


Fig. 17 Momentum thickness Reynolds numbers extracted from maximum heating and pressure CFD Solutions.

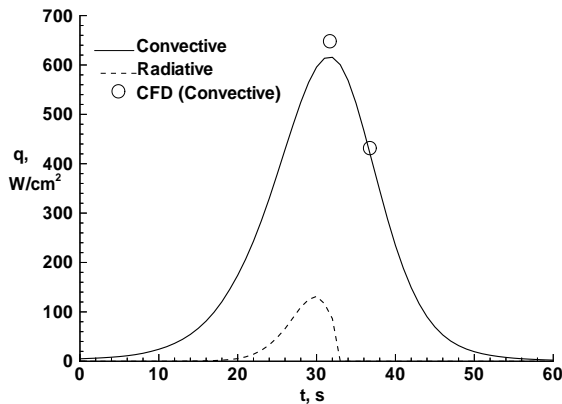


Fig. 15 Estimate of convective and radiative heating at the stagnation point

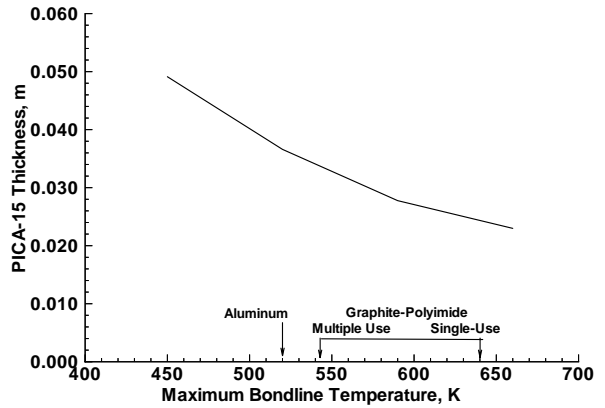


Fig. 18 Relationship between heat shield thickness and maximum temperature experienced by the underlying structure.

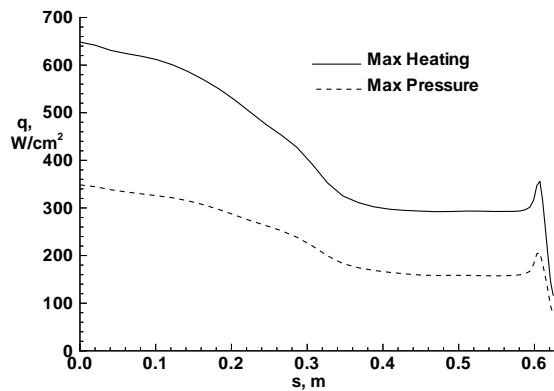


Fig. 16 Nonablating, laminar, forebody heating at maximum heating and pressure trajectory points from LAURA CFD

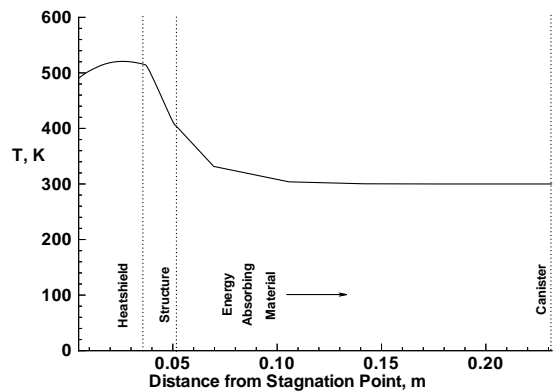


Fig. 19 Temperature distribution across heatshield, structure, and energy absorbing material at time of ground impact.